THE ASTROPHYSICAL JOURNAL, 422:799–809, 1994 February 20

AN X-RAY SPECTROSCOPIC STUDY OF THE PRE-ECLIPSE DIPS OF HERCULES X-1

C. S. CHOI,[1,2] F. NAGASE,[1] F. MAKINO,[1] T. DOTANI,[1] AND K. W. MIN[3]

Received 1992 July 23; accepted 1993 August 26

ABSTRACT

The X-ray binary pulsar Her X-1 was observed with *Ginga* on 1988 August 28 during the orbital phase of 0.76 to 0.85 in the main-on state of the 35 day cycle. During the observations the X-ray intensity varied by a factor of 5 or more on a time scale as short as 30 s, due mostly to the soft X-ray absorption in the pre-eclipse dip phase. From studies of pulse profiles and energy spectra, we find that there exists in the dip phase an unpulsed component which is $\sim 3\%$ of the intensity of the nonabsorbed high level. We suggest that scattering of the source continuum by the optically thin hot corona is responsible for the unpulsed component. In the spectral analysis, we find that the high-state nonabsorbed spectra can be fitted by a power law without absorption, and the spectra observed in the different absorption states can be fitted by two power-law components with the same photon index. An iron-K emission line is required in both cases. The estimated equivalent width of the iron line varies from 0.18 to 0.55 keV in correlation with the change in the absorption column density along the line of sight. We suggest that the fluorescent iron line arises in a cool and relatively small region, like the Alfvén surface, and may be partially intercepted by the optically thick gas cloud passing across the line of sight.

Subject headings: binaries: eclipsing — stars: individual (Hercules X-1) — X-rays: stars

1. INTRODUCTION

Hercules X-1 is an eclipsing binary X-ray pulsar with a low-mass companion. Its $1^d.7$ orbital period and $1^s.24$ X-ray pulsation were revealed with the *Uhuru* satellite (Tananbaum et al. 1972), as well as the 35^d recurrence of the X-ray intensity turn-on (Giacconi et al. 1973). Soon after the *Uhuru* discoveries, the optical counterpart of Her X-1 was identified to be HZ Herculis by detecting both the $1^d.7$ orbital modulation and the $1^s.24$ pulsations in the optical light curve (Bahcall & Bahcall 1972; Davidsen et al. 1972; Forman, Jones, & Liller 1972). The orbital parameters derived by Tananbaum et al. (1972) were improved by Deeter, Boynton, & Pravdo (1981) by combining the pulse arrival time data of *Uhuru* observations with those of the following observations with *OSO 8*, *HEAO 1*, and *Einstein*, thus yielding a precise mass function of $0.8510 \pm 0.0001\ M_\odot$. The pulse period history of Her X-1 over the past 20 years shows on average a secular spin-up with superposed irregular wavy fluctuations (see, e.g., Joss et al. 1977 and Nagase 1989). Long-term monitoring of Her X-1 from *Uhuru* to *Ginga* has revealed a decrease of orbital period with a rate of $\dot{P}_{\rm orb}/P_{\rm orb} = -1.32 \times 10^{-8}\ {\rm yr}^{-1}$ (Deeter et al. 1991). An episode of extended low state was recorded with the *EXOSAT* observations (Parmar et al. 1985).

Many optical studies have been made for the Her X-1/HZ Her system since the discovery of optical pulsations from the system. From photometric observations, HZ Her is suggested to fill its Roche lobe, and its spectral type varies from late A to early B over the orbital period due to the X-ray heating of the companion atmosphere (Bahcall & Bahcall 1972; Boynton et al. 1973; Milgrom & Salpeter 1975a, b; Deeter et al. 1976; Gerend & Boynton 1976). Optical pulsations have also been detected in the emission lines and the $1^d.7$ orbital modulation of the velocity curve was measured (Crampton & Hutchings 1974; Hutchings et al. 1985). The analysis of the optical pulses, together with the X-ray timing results, is used to determine the stellar parameters in the Her X-1/HZ Her system: the companion mass $M_{\rm opt} = 2.0\ M_\odot$, the companion radius $R_{\rm opt} = 3.9\ R_\odot$, and the stellar separation $a = 8.6\ R_\odot$ (Crampton 1974; Middleditch & Nelson 1976; Deeter et al. 1981; Hutchings et al. 1985). A detailed analysis of the optical data suggests a characteristic 35^d modulation of the optical pulsation amplitudes, which is interpreted in the light of episodic mass transfer and obscuration by a tilted accretion disk which undergoes one cycle of retrograde progression every 35^d (Middleditch & Nelson 1976; Middleditch 1983). From *IUE* spectroscopy, Howarth & Wilson (1983) suggested that the UV emission lines originate in discrete blobs of material orbiting at the rim of the accretion disk.

The 35^d cycle variations of X-ray intensities in Her X-1 is considered to be due to precession, although it is unclear what is precessing and why (e.g., Priedhorsky & Holt 1987). Various models have been proposed: a precessing, tilted accretion disk in the tidal field by the companion star (Katz 1973); a disk slaved to the companion star precession (Roberts 1974); a free precessing neutron star (Trümper et al. 1986); precession of the edge of the accretion disk due to mass transfer feedback (Boynton et al. 1980).

In addition to the 35^d recurrence cycle of the high state of X-ray intensity, lasting $\sim 10^d$, it has been known since the early observations with *Uhuru* (Giacconi et al. 1973) that Her X-1 exhibits a decrease of X-ray intensity at orbital phase, $\Phi_{\rm orb} = 0.6$–0.9 (the so-called "pre-eclipse dip"; hereafter the dip) prior to the eclipse and at $\Phi_{\rm orb} = 0.3$–0.6 ("the anomalous dip"). Giacconi et al. (1973) also found that the dips change their phases with respect to the $1^d.7$ eclipse within the main-on state. Jones & Forman (1976) detected a small hump of X-ray intensity with a duration of $\sim 5^d$ at phases 0.5–0.6 of the 35^d cycle (the so-called "short-on" state). From the progression of the dips in successive orbits, Crosa & Boynton (1980) derived the

[1] The Institute of Space and Astronautical Science, 1-1 Yoshinodai 3-chome, Sagamihara, Kanagawa 229, Japan.
[2] Korea Astronomy Observatory, 36-1 Whaam-dong Daejeon 305-348, Korea.
[3] Department of Physics, Korea Advanced Institute of Science and Technology, 373-1 Gusong-dong, Taejeon 305-701, Korea.

recurrence period of $P_r \approx 1^d.62$. The five distinct states, the main-on, the short-on, the low state, the eclipse, and the pre-eclipse dip, has been confirmed with *HEAO* 1 experiment (Gorecki et al. 1982).

Many spectral observations have been made mainly during the high-on state and revealed some interesting features in Her X-1. Pulse phase–dependent changes of spectra were observed in the high-energy (>20 keV) continuum of Her X-1 (Pravdo et al. 1978b). Pravdo et al. (1977a, 1978a) discovered an emission line feature at ~6.4 keV that is ascribed to the iron fluorescent line during both the high-on state and the low state of Her X-1. The 6.4 keV iron line emission was confirmed by observations with the gas scintillation counters aboard *Tenma* (Ohashi et al. 1984). A cyclotron line feature was discovered by Trümper et al. (1978) at around 35–45 keV and this feature was confirmed by further balloon experiments (Gruber et al. 1980; Tueller et al. 1984). Alternative interpretations of the ~35 keV absorption line features have been discussed by Voges et al. (1982) and Soong (1990). Mihara et al. (1990) interpreted the 35 keV absorption feature obtained with *Ginga* as due to cyclotron resonant scattering. Energy spectra with good statistics during the low state were obtained by *Ginga* observations and interpreted as the scattering by the accretion disk and corona extended above the disk (Mihara et al. 1991).

It is noted that recurrent intensity dips are not unique to Her X-1, but widely observed from many low-mass X-ray binaries (see, e.g., Mason 1986 and references therein); some of them show a clear correlation between the orbital period and the dip recurrence period, such as EXO 0748−676 (Parmar et al. 1986). Thus the investigation of intensity dips in the X-ray pulsar Her X-1 might share same common physics with those in the low-mass X-ray binaries and enable us to understand the behavior of an accretion disk; the spectroscopic study of dips in Her X-1 may provide a useful clue for the purpose. There is, however, little spectral observations during the dips of Her X-1. Ushimaru et al. (1989) observed a soft-excess spectrum during the dips and interpreted the spectrum as leaky absorption from clumpy blobs. Mihara et al. (1991) analyzed the dip spectrum in comparison with the low state data and found that it can be reproduced by the sum of a soft component and the absorbed direct beam of the pulsar.

In this paper we present the results of our detailed spectroscopic analysis of the data obtained with *Ginga* during the pre-eclipse phase of Her X-1 in 1988 August.

2. OBSERVATION AND RESULTS

We observed Her X-1 with the Large Area Counters (LAC) aboard *Ginga* (Makino et al. 1987; Turner et al. 1989) four times in 1988 August and September (see Mihara et al. 1991 for the journal of the observations). The LAC consist of eight modules of multicell proportional counters with a total effective area of 4000 cm^2. The LAC cover the energy range from 1 to 37 keV with 48 pulse height channels in the data mode MPC1 and MPC2 and have an energy resolution of 18.0% at 6 keV.

We analyzed in detail the data obtained during the period from 16:07 to 19:38 (UT) on 1988 August 28. These data were obtained in the MPC2 mode with a time resolution of 62.5 ms (high-bit rate telemetry). Background was subtracted using the method described in Hayashida et al. (1989). Long-term monitoring of Her X-1 by the all-sky monitor (Tsunemi et al. 1989) onboard *Ginga* showed that Her X-1 was in the main-on state on August 28 (Mihara et al. 1991). The phase in the 35 day cycle and the orbital phase of the present observations were calculated to be $\Psi_{35} = 0.1 \pm 0.03$ and $\Phi_{orb} = 0.76$–0.85, respectively, using the ephemeris presented by Deeter et al. (1991). We analyzed these data because pre-eclipse dips were expected just at this orbital phase of the data.

2.1. *Light Curve*

X-ray light curves in four energy bands are shown in Figure 1 together with the softness ratio (uppermost panel); i.e., ratio of the X-ray flux in 1.2–4.6 keV to that in 6.9–11.5 keV. The X-ray flux observed is typically 7.5×10^{-9} ergs cm^{-2} s^{-1} in the energy range of 1.2–36.8 keV except for the period of dips. This flux corresponds to an X-ray luminosity of 2.1×10^{37} ergs s^{-1} assuming the distance to Her X-1 to be 5 kpc (Bahcall 1978). This high luminosity, which is typical of the peak of the main high-on state in the 35 day cycle, confirms that Her X-1 is actually in the main-on state.

As expected from the orbital ephemeris of the current observation, we see drastic intensity variations, especially in the lowest (1.2–4.6 keV) energy band as shown in Figure 1. It is notable that the time scales of variations range widely from 30 s to more than 10 minutes. These variations are considered to be a property of the pre-eclipse dips. The dip is deepest at low energy and is basically consistent with the phenomena due to X-ray absorption by cold matter, as already noticed by many authors (Ohashi et al. 1984; Ushimaru et al. 1989; Mihara et al. 1991).

2.2. *Energy Spectrum*

We classified the data shown in Figure 1 into six groups (data sets I–VI) according to the flux level to see how the energy spectrum changes. The pulse height spectra calculated for each group are shown in Figure 2*a* in order of decreasing flux level. The spectral change show strong energy dependence as expected from the absorption by cold matter. However, data sets I–VI have relatively flat spectra below 4 keV, which is inconsistent with the absorption by homogeneous cold matter. This feature of the soft excess flux is already reported in the previous works (Ushimaru et al. 1989; Mihara et al. 1991).

This feature is visible more clearly in Figure 2*b*, in which the count rate ratio (PHA ratio) in each pulse height channel is taken between data sets II–VI and data set I. The solid lines in Figure 2*a* and 2*b* show X-ray absorption feature due to matter of column density 1×10^{24} H-atoms cm^{-2}. It is noticed from Figure 2*b* that the PHA ratio of data sets V and VI is almost flat at energies below 4 keV. Because the energy spectrum of data sets V and VI below 4 keV is dominated by the soft excess component, this means that the spectral shape of the soft excess component below 4 keV is almost same as that of data set I. In other words, this soft excess component is not subjected by any additional absorption over that of direct component. It is known that the spectrum of the main-on state, such as data set I, suffer from little absorption (Mihara et al. 1991). Therefore, the soft excess component also seems to suffer from little absorption. The soft excess flux correspond to ~3% of the flux of data set I.

It is also evident from Figure 2*b* that the intensity at ~20 keV decreases gradually to ~40% of the intensity of data set I, with absorption increasing from data sets II to VI. The spectral changes in data sets II–VI at energies 4–10 keV can be explained by photoelectric absorption with increasing column density. Whereas the decrease of intensity without energy dependence at energies above ~18 keV cannot be explained by

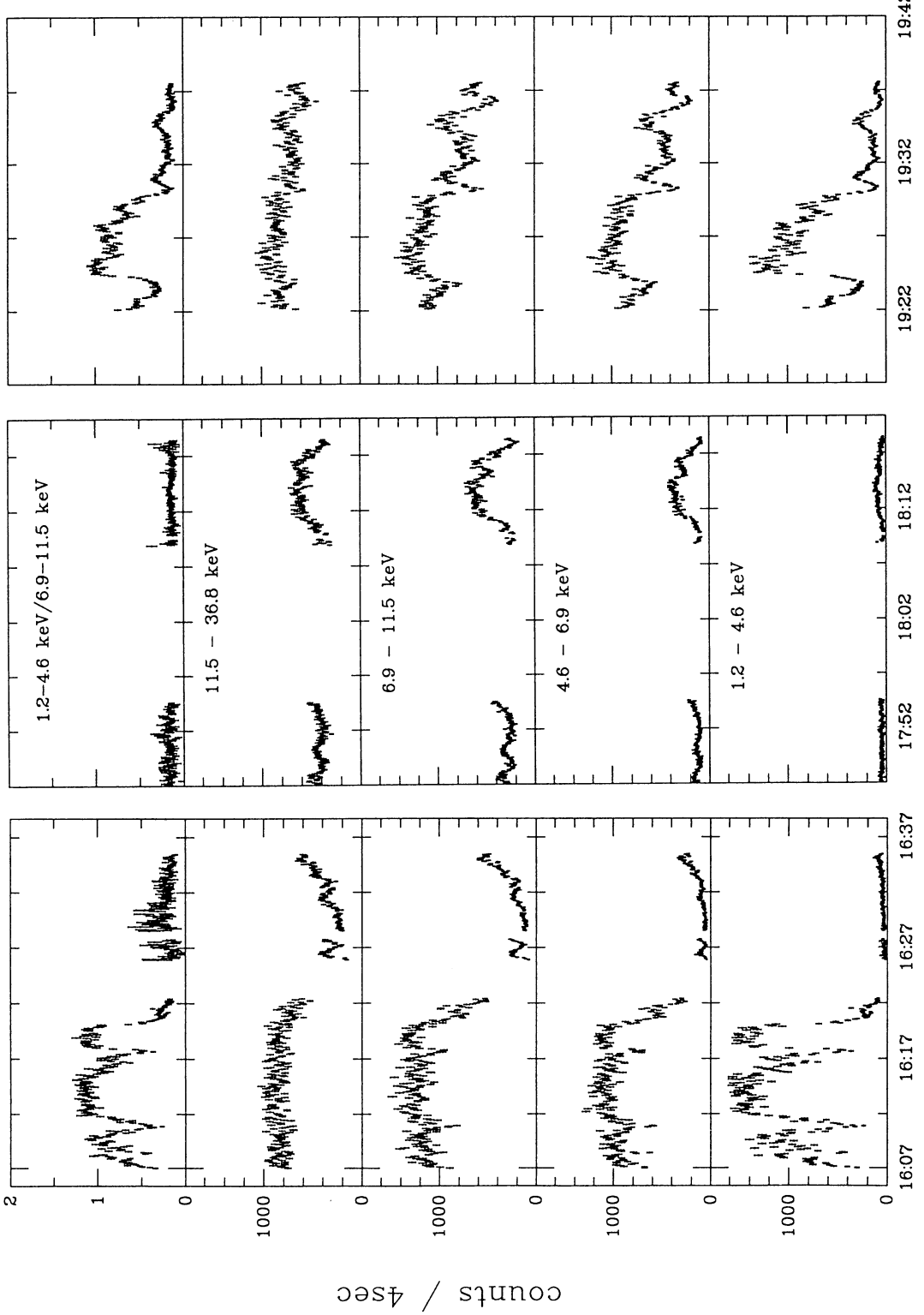

FIG. 1.—X-ray light curves in four energy bands observed with *Ginga* in 1988 August. The intensities of each bin result from 4 s accumulation after background subtraction and aspect correction. The softness ratio (of the 1.2–4.6 keV flux to the 6.9–11.5 keV flux) is plotted in the top panel.

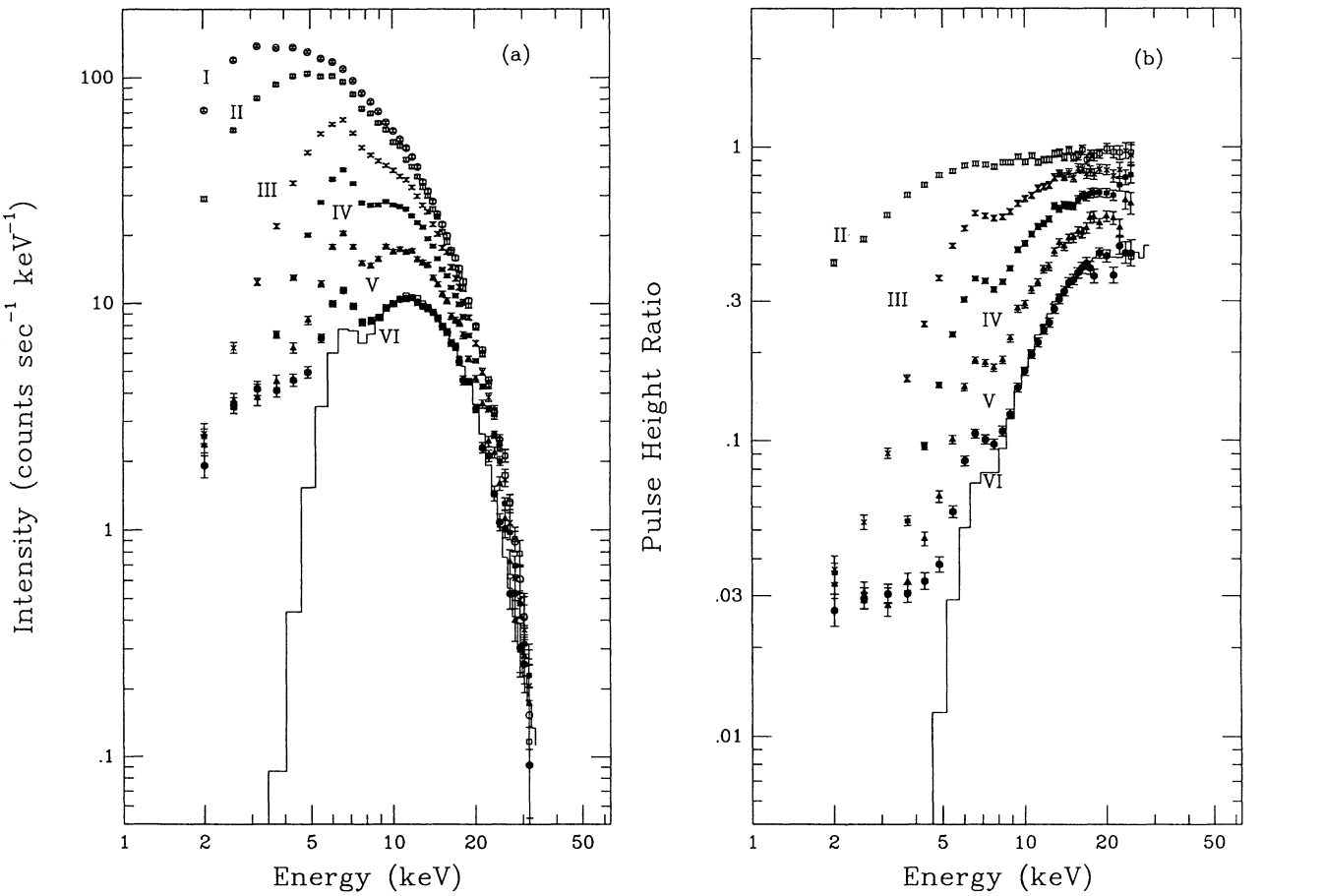

FIG. 2.—(*a*) Pulse height spectra of Her X-1 observed with *Ginga* during the pre-eclipse dip phase in 1988 August. The six spectra (I–VI) are shown decreasing order of intensity, which is the order of increasing absorption measure. (*b*) The ratio of count rate for each pulse height channel between the spectra II–VI and the spectra I, which do not show significant absorption. Solid lines in the figures display X-ray absorption feature due to matter of column density 1×10^{24} H atoms cm^{-2}, in which both the effects of photoelectric absorption and Thomson scattering are included.

the photoelectric absorption but can be explained by the escape of photons due to electron scattering by intervening matter in the line of sight. In fact, the solid curve in Figures 2*a* and 2*b* (which include both the effects of photoelectric absorption and Thomson scattering) explain both the change of spectral shape in 4–10 keV and the intensity decrease at energies above ~18 keV.

2.3. *Pulse Profile*

Energy dependent pulse profiles are obtained for individual data sets using the pulse folding technique. Examples are shown in Figure 3 for the main-on data (I) and the dip data (VI). Pulse shapes of data set I are typical in the main-on high state characterized by a small interpulse and a double-peak in the main pulse (Pravdo et al. 1977b; Soong et al. 1987; Ushimaru et al. 1989; Soong et al. 1990). The pulse profiles in the dip are similar to those in data set I above ~5 keV, but the pulse becomes almost invisible below ~5 keV. This confirms the earlier results (Ohashi et al. 1984; Mihara et al. 1991).

We define the root-mean squared (rms) pulse amplitude $A_{\rm pulse}$ to get quantitative results for the pulse amplitude:

$$A_{\rm pulse} = \frac{1}{\bar{n}} \left\{ \frac{\sum_i [(n_i - \bar{n})^2 - \sigma_i^2]}{N} \right\}^{1/2}, \qquad (1)$$

where n_i, $\bar{n}$, σ_i, N are the count rate of ith bin, the phase-averaged count rate, the statistical fluctuation of the count rate, and the number of bins, respectively. The pulse fraction calculated for each data set are shown in Figure 4. The increase of pulse fraction with energy is clearly seen in the figure.

The pulse profiles in Figure 3, together with the pulse fraction in Figure 4, reveal the following features of the profile change in the dips: (1) no significant pulsations are seen below ~4 keV, (2) the pulse fraction above ~10 keV is almost the same for all data sets, although the pulse amplitude itself is different, and the pulse profile in the dip (e.g., right panel of Fig. 3) is same as that out of the dip (e.g., left panel of Fig. 3) suggesting little smearing, (3) a reduced pulse fraction and a little smearing are seen in the middle energy band of 4–10 keV. Fact 1 suggests that the soft excess flux is not due to the leakage of direct beam through inhomogeneous matter but due to scattering by extended thin plasma.

3. SPECTRAL ANALYSIS

We have given an overview of the spectral changes, which occurred during the dips, in the previous section and have clarified qualitatively the properties of the dip spectra. To investigate further and quantitatively the properties of the dips, we constructed 43 time-sliced energy spectra. The accumulation time of each spectrum was selected so that the intensity and softness ratio (see Fig. 1) in an integration period were

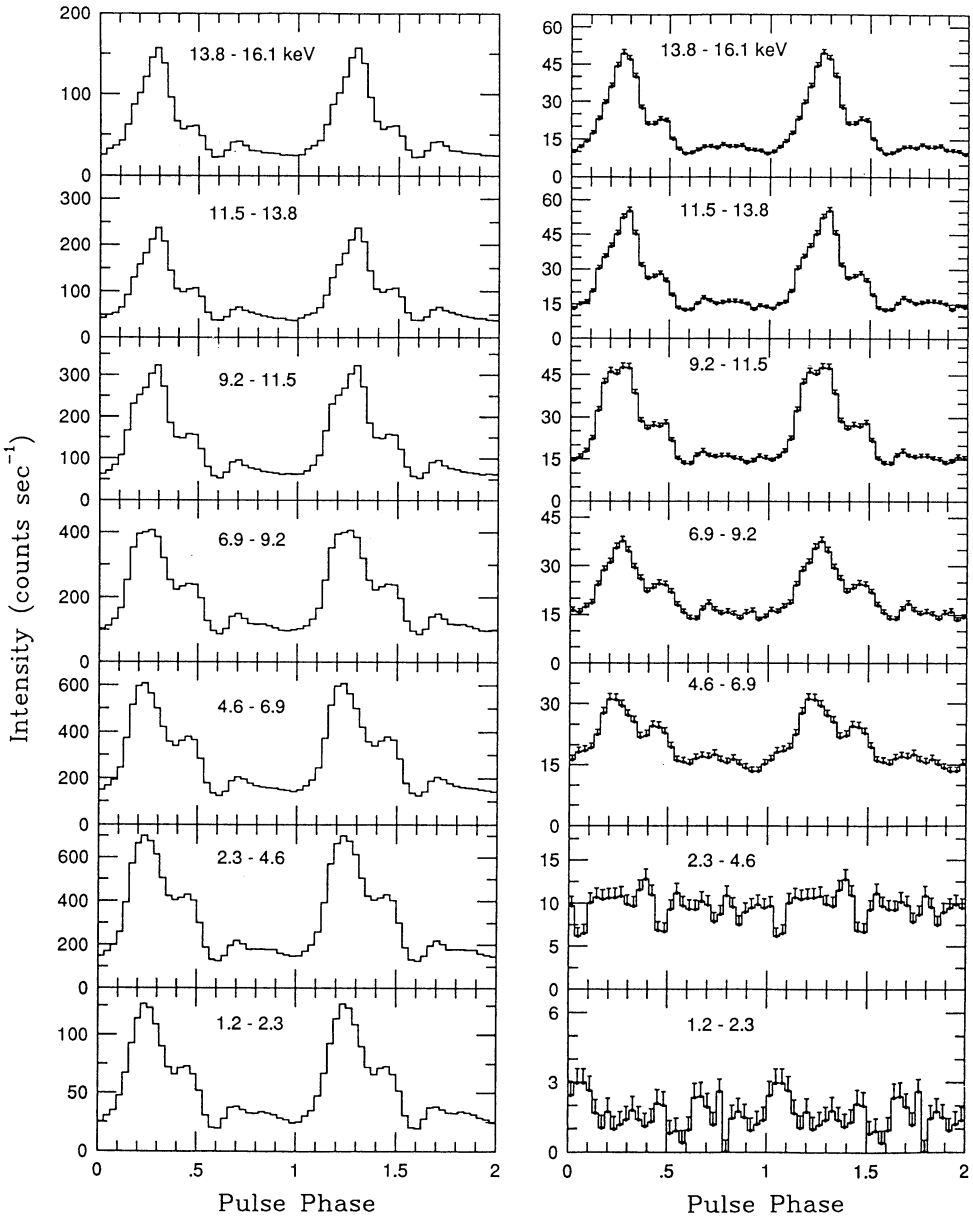

FIG. 3.—Pulse profiles in two intensity levels folded modulo the pulse period of 1.23776 s (for seven energy bands in the range 1.2–16.1 keV) after background subtraction. The profiles on the *left* correspond to data set I, the highest intensity level, and the *right* to the lowest intensity level (data set VI).

approximately constant. The typical integration time for individual spectrum ranges from 40 to 150 s.

A typical spectrum of Her X-1 in the high state has a shape common to X-ray pulsars and can be represented by the conventional model spectrum of a power law with a high-energy cutoff (e.g., White et al. 1983). It was revealed from recent studies with *Tenma* and *Ginga* (Makishima et al. 1990; Mihara et al. 1990; Makishima & Mihara 1992) that the turnover feature at high energies is related to cyclotron resonant scattering, and the observed cyclotron resonance features can be better fitted by a function with a form of resonant absorption. In the following analysis, however, we adopt the conventional representation of an exponential cutoff because the present time-sliced spectra do not have enough statistics at high energies to resolve the difference of the resonant absorption feature and the exponential cutoff.

3.1. *Fitting of the Dip Spectra*

Although a spectrum affected less by absorption (as shown in data set I of Fig. 2*a*) can be fit by the above model, it is clear from the analysis in the previous section that we need another component to fit the soft component in the spectrum. We assume that the soft excess component has the same spectral shape with that of main-on state because the component may originate from X-ray scattering. Therefore, we need to take into account the following two components to model the spectrum; one is the direct component, which shows pulsations and is sometimes heavily absorbed, and the other is the unabsorbed

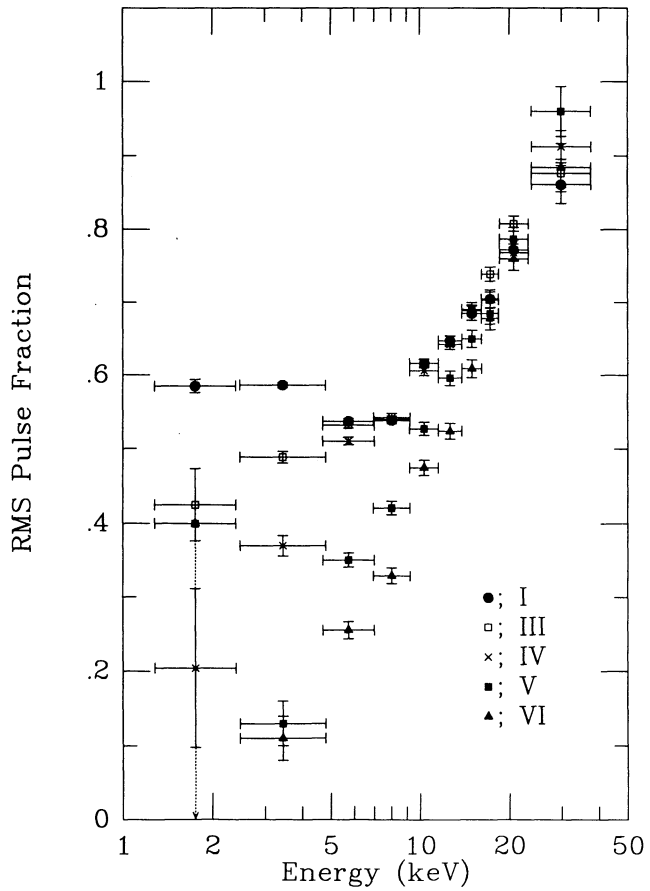

FIG. 4.—Root-mean squared fractions of pulse in Her X-1 plotted against energy. Different symbols correspond to the different data sets I–VI in Figure 2. Upper limits (*dashed line*) and errors are in 1 σ level.

component, which shows no pulsations and has the same spectral shape as that of the nonabsorbed direct component. This unabsorbed component corresponds to the soft component. In fact, we found that the following model of two component continua and an iron emission line can reproduce the observed spectra in the dip phase for different degrees of absorption. The function which we adopted in the fitting is

$$I(E) = \begin{cases} A_1 E^{-\alpha} \exp(-\sigma N_{\rm H}) + A_2 E^{-\alpha} + I_{\rm Fe} & (E \le E_c), \\ [A_1 E^{-\alpha} \exp(-\sigma N_{\rm H}) + A_2 E^{-\alpha}] & \\ \quad \times \exp[-(E - E_c)/E_f] + I_{\rm Fe} & (E > E_c), \end{cases} \quad (2)$$

where A_1, A_2, E_c, and E_f represent the normalization coefficient of the direct component, that of the unabsorbed component, and the cutoff and *e*-folding energies, respectively. The formula is the same as that of the partial covering model. Since it was revealed in the previous section that the soft component seems to suffer from little absorption (the amount is insignificant within the statistical accuracy of data), we did not apply absorption for the second term (the interstellar column density towards Her X-1 is negligible for the *Ginga* energy range). This is the reason that we use an unabsorbed component there. The parameters α, E_c, and E_f of the unabsorbed component are assumed to have the same values as those of the direct component; this assumption is based on the analysis in the previous section. The parameters $\sigma(E)$ and $N_{\rm H}$ are the absorption coefficient by cold interstellar matter and the hydrogen equivalent column density, respectively. The iron line is represented by a Gaussian form:

$$I_{\rm Fe}(E) = \frac{A_{\rm Fe}}{\sqrt{2\pi}\Gamma} \exp\left[-\frac{(E - E_{\rm K})^2}{2\Gamma^2}\right], \quad (3)$$

where $A_{\rm Fe}$ is the iron line intensity, $E_{\rm K}$ the line center energy, and Γ the intrinsic line width. We assume that the width of the iron line is far smaller than the resolution of the LAC counter and fix $\Gamma = 0.1$ keV in the fitting. In the present model, we set the absorption for iron line to zero. It is, of course, expected that some degree of absorption occurs for the iron line (at least self-absorption of the reprocessing matter should be taken into account), which is probably different from that of continuum X-rays because the emission sites are different. However, it is difficult to determine the absorption for the iron line from the fitting, since it depends on the geometry of the reprocessing site to be assumed. Therefore, we decided to set the absorption for iron line to zero in the model and to consider it separately in the next subsection. For the interstellar/circumstellar absorption, we apply in the present fitting the absorption coefficient $\sigma(E) = \sigma_{\rm MM}(E) + \sigma_{\rm T}(E)$, involving both the photoelectric absorption $\sigma_{\rm MM}(E)$ and the Thomson scattering $\sigma_{\rm T}(E)$ for attenutation of the X-rays from the source. The Thomson scattering is dominant for the X-ray attenuation above $\sim$15 keV and is consistent with the energy independent decrease of X-rays as described in §§ 2.2 and 2.3. For the photoelectric absorption coefficient, we adopt the cross section compiled by Morrison & McCammon (1983). When the absorption of the direct component is negligible, we did not include the unabsorbed soft component in the model (A_2 was set to zero) because the spectral shape of the direct component and the unabsorbed component become identical and the two components become indistinguishible.

Thus the spectral fitting has been carried out with seven (for the high-state spectra) or eight (for the dip spectra) free parameters using the model described in equations (2) and (3). We tried to fit all 43 energy spectra, but some of them did not give useful results due mainly to poor statistics. This is caused by time slices which are too short, during intervals of rapid intensity variations. Hence we summarize the results in Table 1 for the 21 spectra which gave meaningful results. The equivalent width of the iron line, designated as EW in Table 1, is evaluated as

$$\mathrm{EW} = \frac{A_{\rm Fe}}{A_1 E_{\rm K}^{-\alpha} \exp[-\sigma(E_{\rm K}) N_{\rm H}] + A_2 E_{\rm K}^{-\alpha}} \ \mathrm{keV}. \quad (4)$$

Note that the cutoff energy E_c is always higher than the line center energy $E_{\rm K}$. Examples of the fits are shown in Figure 5 for four spectra with various flux level. Figure 6 shows the best-fit parameters, relating to the iron line, plotted against the orbital phase. The photon flux of the direct component in Figure 6*a* is estimated by integrating the first term of equation (2) in the energy range 7.1–35 keV, using the best-fit parameters without absorption. The derived line center energy and the equivalent width are also plotted in Figures 6*d* and 6*e*, respectively.

From the results shown in Figures 5 and 6 and summarized in Table 1, we see the following properties of the dip spectrum in Her X-1: (1) the direct component suffer from absorption with column density ranging from $N_{\rm H} \le 10^{22}$ to $N_{\rm H} = 1.2 \times 10^{24}$ H-atoms cm^{-2} during the present observations

TABLE 1

BEST-FIT PARAMETRES FOR TIME-SLICED ENERGY SPECTRA[a]

Number	Φ_{orb}	A_1[b]	α	log N_H[c]	E_c[d]	E_f[d]	A_2[b]	A_3[e]	E_K[d]	EW[d]	χ^2_ν (d.o.f.)
1.....	0.7639	483.3 ± 92.5	0.86 ± 0.08	22.66 ± 0.10	18.0 ± 1.6	11.7 ± 3.3	...	16.6 ± 7.5	6.53 ± 0.26	0.19 ± 0.09	0.97 (36)
2.....	0.7643	514.5 ± 32.2	0.88 ± 0.03	22.03 ± 0.08	18.9 ± 0.8	9.1 ± 1.5	...	20.1 ± 4.6	6.48 ± 0.14	0.20 ± 0.05	1.16 (38)
3.....	0.7649	484.7 ± 101.6	0.85 ± 0.08	22.93 ± 0.07	18.4 ± 1.3	9.8 ± 2.6	...	17.9 ± 7.4	6.34 ± 0.22	0.22 ± 0.09	1.24 (36)
4.....	0.7652	580.1 ± 57.3	0.91 ± 0.04	22.25 ± 0.13	18.0 ± 0.9	10.3 ± 1.7	...	19.7 ± 5.5	6.37 ± 0.16	0.19 ± 0.05	0.95 (36)
5.....	0.7656	580.5 ± 8.9	0.91 ± 0.01	≤21.5	19.3 ± 0.5	8.1 ± 0.9	...	19.9 ± 3.6	6.50 ± 0.12	0.19 ± 0.03	0.98 (38)
6.....	0.7664	590.7 ± 27.5	0.92 ± 0.02	≤21.5	19.2 ± 0.6	8.9 ± 1.2	...	20.4 ± 4.1	6.32 ± 0.13	0.19 ± 0.04	1.29 (38)
7.....	0.7682	619.9 ± 28.1	0.93 ± 0.02	21.24 ± 0.33	19.0 ± 0.6	8.8 ± 1.1	...	20.0 ± 3.9	6.53 ± 0.13	0.19 ± 0.04	1.40 (38)
8.....	0.7692	561.1 ± 128.8	0.93 ± 0.08	23.36 ± 0.05	20.4 ± 0.9	7.7 ± 1.6	45.4 ± 7.3	12.4 ± 4.2	6.45 ± 0.17	0.19 ± 0.06	0.95 (37)
9.....	0.7696	360.7 ± 49.2	0.76 ± 0.05	23.55 ± 0.04	18.8 ± 1.1	9.3 ± 2.1	25.2 ± 3.9	11.1 ± 3.8	6.32 ± 0.20	0.26 ± 0.09	1.29 (37)
10.....	0.7714	244.0 ± 14.1	0.65 ± 0.02	23.97 ± 0.02	16.7 ± 0.9	12.3 ± 1.9	13.1 ± 1.1	3.5 ± 1.2	6.25 ± 0.22	0.33 ± 0.11	1.05 (37)
11.....	0.7724	257.7 ± 17.3	0.67 ± 0.02	24.08 ± 0.02	19.0 ± 0.8	7.9 ± 1.6	11.4 ± 0.9	4.0 ± 1.0	6.45 ± 0.16	0.55 ± 0.14	1.13 (37)
12.....	0.7733	277.2 ± 39.6	0.64 ± 0.05	24.00 ± 0.02	18.5 ± 0.8	8.8 ± 1.4	13.9 ± 1.3	5.0 ± 1.3	6.29 ± 0.15	0.46 ± 0.12	0.77 (37)
13.....	0.7751	470.6 ± 32.0	0.80 ± 0.02	23.72 ± 0.03	19.4 ± 1.2	8.1 ± 2.3	23.7 ± 3.7	12.3 ± 4.3	6.29 ± 0.21	0.36 ± 0.13	0.75 (37)
14.....	0.8063	378.2 ± 48.5	0.77 ± 0.04	23.91 ± 0.02	18.8 ± 0.8	8.1 ± 1.4	15.9 ± 1.6	3.6 ± 1.5	6.58 ± 0.24	0.21 ± 0.09	1.27 (37)
15.....	0.8136	614.7 ± 24.4	0.90 ± 0.01	23.91 ± 0.01	20.6 ± 0.6	6.2 ± 1.1	13.9 ± 1.5	8.3 ± 1.5	6.51 ± 0.11	0.44 ± 0.08	1.10 (37)
16.....	0.8159	566.7 ± 162.2	0.89 ± 0.09	23.66 ± 0.04	19.4 ± 0.7	8.8 ± 1.3	17.7 ± 3.1	7.6 ± 2.3	6.34 ± 0.15	0.20 ± 0.06	1.33 (37)
17.....	0.8166	394.0 ± 130.6	0.76 ± 0.10	23.84 ± 0.03	18.1 ± 0.8	9.5 ± 1.5	13.8 ± 2.4	8.6 ± 1.9	6.39 ± 0.12	0.42 ± 0.09	1.23 (37)
18.....	0.8458	590.8 ± 48.2	0.93 ± 0.03	22.69 ± 0.04	19.9 ± 0.7	9.2 ± 1.3	...	16.6 ± 3.8	6.27 ± 0.13	0.18 ± 0.04	1.01 (36)
19.....	0.8464	371.5 ± 86.2	0.79 ± 0.08	23.30 ± 0.05	18.9 ± 0.9	9.4 ± 1.6	28.1 ± 6.0	11.8 ± 4.0	6.29 ± 0.18	0.20 ± 0.07	1.31 (37)
20.....	0.8474	607.3 ± 108.1	0.93 ± 0.06	23.47 ± 0.03	19.2 ± 0.8	9.2 ± 1.5	20.7 ± 3.8	13.9 ± 3.2	6.42 ± 0.12	0.25 ± 0.06	1.10 (37)
21.....	0.8488	375.2 ± 237.4	0.78 ± 0.19	23.58 ± 0.09	20.6 ± 1.8	8.1 ± 3.1	15.0 ± 6.6	11.6 ± 5.2	6.13 ± 0.24	0.32 ± 0.14	0.83 (37)

[a] Quoted errors are 90% confidence limits for a single parameter.
[b] A_1 and A_2 are the coefficients of continuum spectra normalized at 1 keV in untis of photons s^{-1} keV^{-1}.
[c] N_H is an absorption column density in units of H atoms cm^{-2}.
[d] Cutoff energy E_c, folding energy E_f, iron line energy E_K and equivalent width EW are presented in units of keV.
[e] A_3 is the intensity of iron line in units of counts s^{-1}.

($\Phi_{orb} = 0.76$–0.85); (2) the ratio of the unabsorbed flux to the direct component ranges between 2.5% and 7.5%; (3) although the apparent luminosity calculated using the best-fit parameters in 1.7–35 keV varies from 0.5×10^{37} ergs s^{-1} to 2.1×10^{37} ergs s^{-1} for the assumed distance $d = 5$ kpc, absorption-corrected intrinsic luminosity is found to be stable at $L_x = 2.1 \times 10^{37}$ ergs s^{-1} during the observation.

3.2. *Behavior of the Iron Line and the Unabsorbed Component*

We found that the line center energies of iron are all consistent with 6.4 keV (weighted average is $E_K = 6.41 \pm 0.03$ keV). This means that the iron emission line is predominantly due to fluorescence of cold matter. The line intensity and the flux of the unabsorbed component are plotted against the absorption column density (N_H) in Figure 7, together with that of continuum flux above 7.1 keV corrected for the absorption using the best-fit parameters. The continuum flux above 7.1 keV in Figure 7*a* is almost constant around the value of 0.25 photons cm^{-2} s^{-1} (or 5.8×10^{-9} ergs cm^{-2} s^{-1}) in spite of the change in N_H over two orders of magnitude during the short period of the pre-eclipse phase. On the other hand, the intensity of the iron line is constant at ~ 20 counts s^{-1} for $N_H \leq 1 \times 10^{23}$ cm^{-2}, and it decreases to 3.5 counts s^{-1} as N_N increases to 1.2×10^{24} cm^{-2}, as shown in Figure 7*b*. Of course, most of the line intensity decrease is explained by the characteristics of the model function, in which we set the absorption for iron line emission artificially zero. If we assume that the intrinsic iron line intensity is constant and the iron line suffer from the same amount of absorption as the continuum flux, the line intensity would be 2.6 counts s^{-1} for $N_H = 1.2 \times 10^{24}$ cm^{-2}. This value is slightly smaller than the observed value. It may be more appropriate to use the iron line equivalent width to investigate the relation between the line intensity and the continuum flux. The observed iron line equivalent widths are plotted in Figure 8 against the column density N_H. It increases from 0.18 to 0.55 keV as the increase of the column density.

4. DISCUSSION AND CONCLUSION

We observed Her X-1 in 1988 August during the orbital phase $\Phi_{orb} = 0.76$–0.85 at the peak of main-on state of the 35 day cycle. This observation corresponds to the so-called pre-eclipse phase (Crosa & Boynton 1980), and in fact we observed drastic intensity variations on timescales from 30 s to more than 10 minutes. From spectroscopic analysis, we have revealed that the complex intensity variations can be explained in terms of absorption and scattering out of the beamed X-rays by gas clouds passing across the line of sight, plus an additional component which exhibits the same spectral shape as absorption corrected main component and iron emission line at 6.4 keV. Although the apparent luminosity spans $L_x = (0.5$–$2.1) \times 10^{37}$ ergs s^{-1}, in the energy range 1.2–36.8 keV, the absorption-corrected intrinsic luminosity of the source is stable at $L_x = 2.1 \times 10^{37}$ ergs s^{-1} during the observations.

4.1. *Short Timescale Intensity Drop*

Vertical structures of the outer disk rim are expected to produce variations in the light curve because the inclination angle of Her X-1 system is large ($\sim 85°$). When gas inflowing from the inner Lagrangian point falls onto the accretion disk, a turbulent gas structure might be formed over the accretion disk at the impact zone on the disk rim. It is plausible that such a turbulent gas at the impact zone extents vertically at the rim of disk and forms gas clouds of different size and different density. If such gas clouds intersect the line of sight at this special orbital phase of pre-eclipse, it may cause absorption and scattering out of soft X-rays. Adopting the electron density of the cloud $n_e \approx 2 \times 10^{13}$ cm^{-3} as suggested by Howarth & Wilson (1983), we obtain roughly the size of the cloud $R_b \approx$

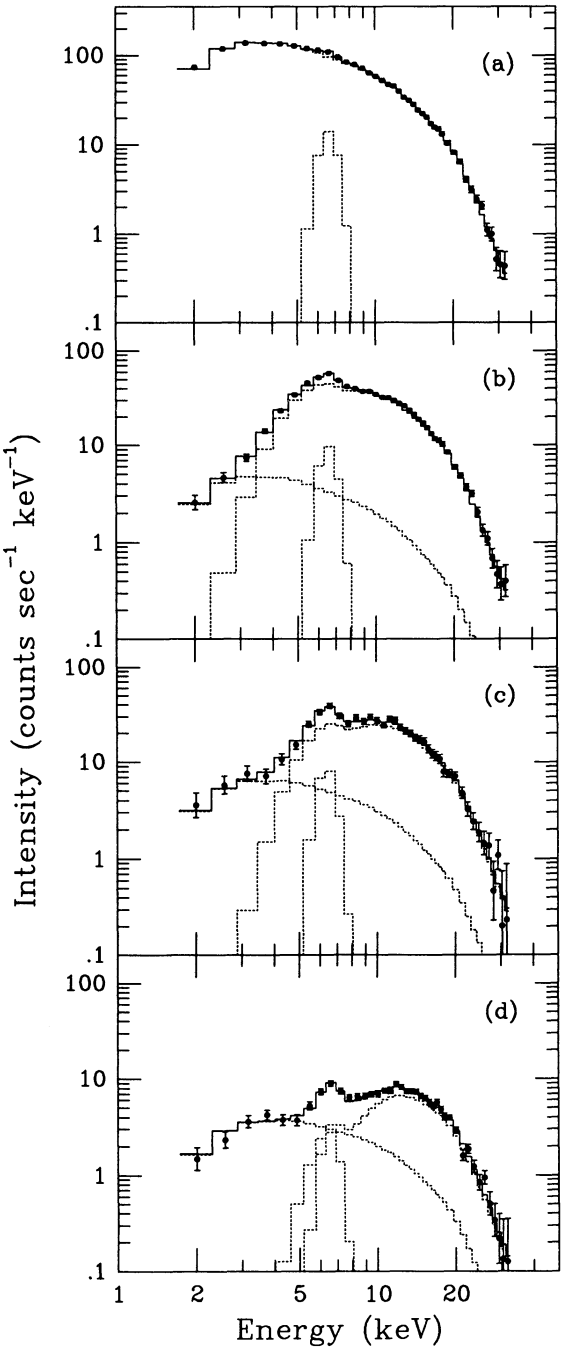

FIG. 5.—Examples of spectral fits are shown for four spectra of different degree of X-ray absorption. The dotted lines are each component of the best-fit model function (two-component continua and an iron emission line; see text for detail) and the solid lines are the sum. Figures (*a*), (*b*), (*c*), and (*d*) correspond to Nos. 5, 20, 13, and 11 of Table 1, respectively.

5×10^{10} cm from the observed maximum column density $N_H \simeq 1 \times 10^{24}$ cm^{-2}. This is about one-tenth of the radius of the accretion disk in Her X-1. It is worth mentioning that Hirose, Osaki, & Mineshige (1991) obtained, from the three-dimensional simulations of an accretion disk, the result that the disk rim is vertically enhanced with a ratio of the vertical height to the disk radius of 0.15 at the orbital phase $\Phi_{orb} \simeq 0.8$.

Short timescale intensity drops seen at the beginning of observation (see Fig. 1) may suggest the formation of blobs with smaller size at the boundary of the cloud region. It may be caused by the vertical turbulence of the perturbations of the outer edge of an accretion disk due to the impact by an inflowing gas stream. It is necessary to resort to the smaller blobs ($r \sim 10^9$ cm), suggested by Bochkarev & Karitskaya (1989), in order to account for the smooth and short time variation of the absorption profile in the light curve shown in Figure 1. They proposed that small blobs can be formed at the impact zone and survive for a time longer than a Keplerian orbit. If we take the Keplerian velocity at the outer rim of an accretion disk to be $V_c \approx 250$ km s^{-1}, the diameter of the blobs is comparable to the duration of the short timescale dips.

4.2. *Soft X-Ray Excess*

We have shown in section 2 that the soft excess component is not due to the leakage of direct beam, as discussed by Ushimaru et al. (1989), but due to the scattering of X-rays from a central source by a thin hot plasma on the basis of the absence of pulsations in this component. Bochkarev (1989) investigated possible existence of the coronal gas around the outer part of the accretion disk, and showed the physical conditions; i.e., the coronal temperature and gas density would be $T_e \approx 2.5 \times 10^6$ K and $n_e \approx 5 \times 10^{11}$ cm^{-3}, respectively. If there is such a corona region, it could be responsible for the scattered soft X-ray component. It would be useful to estimate the electron column density of such a corona along the line of sight. The fraction of the scattered flux (~3%) described in § 3 requires

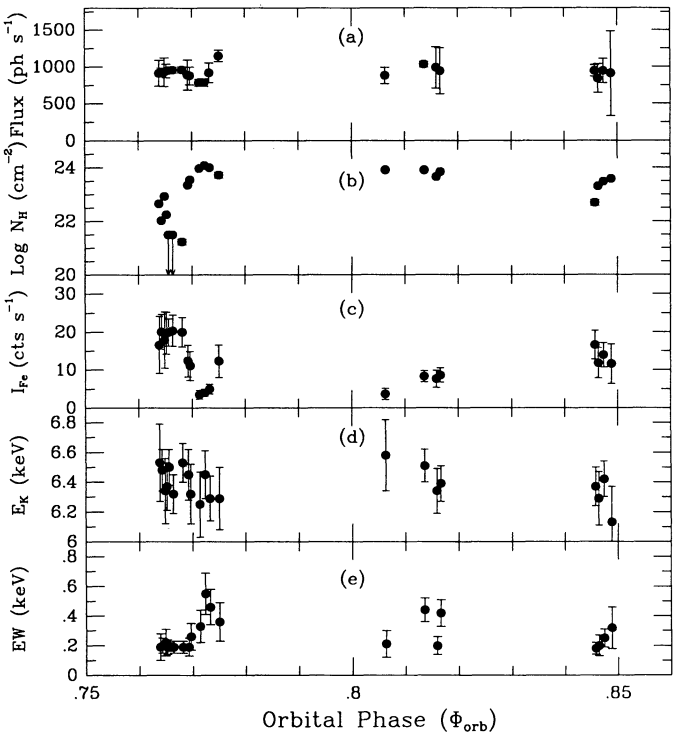

FIG. 6.—Several parameters obtained from the fits for the time-sliced spectra are plotted against the orbital phase: (*a*) intrinsic photon flux in the energy range 7.1–35 keV calculated numerically from eq. (2) without the absorption, using the best-fit parameters obtained, (b) hydrogen equivalent column density of the intervening gas in units of cm^{-2}, (*c*) intensity of the observed iron-K line I_{Fe} in units of counts s^{-1}, (*d*) the line center energy E_K in keV, and (*e*) the equivalent width EW of the iron line in keV.

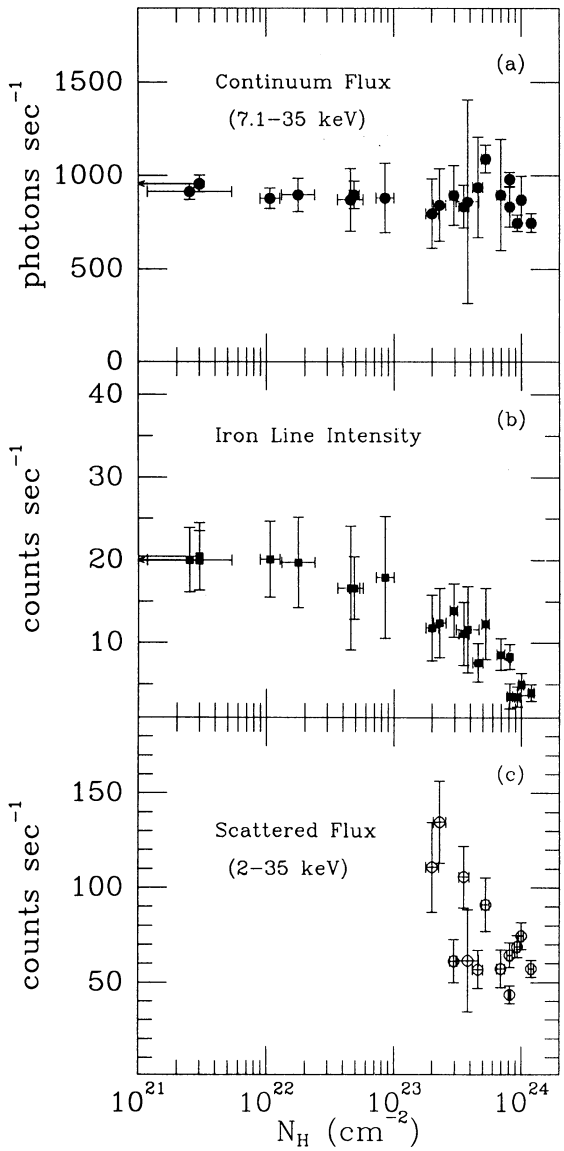

FIG. 7.—(*a*) Continuum flux in the range 7.1–35 keV, (*b*) the iron line intensity, and (*c*) the scattered flux in the energy range 2–35 keV are plotted against the absorption column density N_H.

the column density to satisfy the following equation:

$$N_e \sigma_T (\Omega_c/4\pi) \approx 0.03 , \quad (5)$$

where N_e is the electron column density, and Ω_c the solid angle of the coronal gas subtended by the neutron star. Assuming that the corona is distributed above and below the accretion disk with a solid angle of about half of a sphere ($\Omega_c \approx 2\pi$), an electron column density $N_e \approx 9 \times 10^{22}$ cm^{-2} is required to explain the observed scattered flux if the obscuration of the scattered flux by the gas cloud is negligible. Using the estimated electron density of $n_e \approx 5 \times 10^{11}$ (Bochkarev 1989), we obtain the size of such a corona to be $R \approx 2 \times 10^{11}$ cm. This value is comparable with the height ($\sim 10^{11}$ cm) to which the corona rises, as suggested by Bochkarev (1989).

The low-state spectrum observed with *Ginga* 9 days before this observation was interpreted in terms of two scattered components (Mihara et al. 1991): a soft component due to scattering by thin hot plasma and a hard component due to forward scattering by thick cold matter, both of which were not pulsating. The flux of the soft component that Mihara et al. (1991) has derived is comparable with the soft component we derived from the pre-eclipse dip spectrum. Therefore, the scattering of the soft component in the low state is also explained in the scheme of the above model with the region of hot corona extended over the accretion disk. Although an acceptable fit by free-free emission is obtained for the unabsorbed component, the free-free emission does not account for the emissivity of 3% of total luminosity. The dependence of non-pulsating component on the column density is not clear, because of uncertain flux at low column density. The fluctuation of the flux shown in Figure 7*c* may be due to partial covering of the scattering region by absorbing blobs.

It is noteworthy that the soft excess phenomena have been revealsed for many dipping sources; i.e., Vela X-1 (Haberl & White 1990) and Cen X-3 (Nagase et al. 1992) among the massive X-ray binaries, and EXO 0748−676 (Parmar et al. 1986) and 4U 1254−690 (Courvoisier et al. 1986), etc., among the low-mass X-ray binaries. A photoionized region of stellar wind is considered to be responsible for the X-ray scattering in massive wind-fed binaries, whereas an accretion disk corona (ADC) region will be the site of scattering in the disk-fed low-mass binaries. The soft excess flux revealed in this study from Her X-1 will be due to the ADC scattering, sharing a common feature with the dipping low-mass X-ray binaries.

4.3. *Possible Site of the Line Emission*

It was suggested by Pravdo et al. (1977a) and by Basko (1980) that matter stagnated near the Alfvén surface is responsible for reprocessing iron lines. In addition to this region, an accretion disk surface, outer edge of the accretion disk, and atmosphere of the companion star could be suspected for the line emission. Mihara et al. (1991) observed a broadened iron line together with a nonpulsating continuum emission in the low state. They interpreted the broadening with

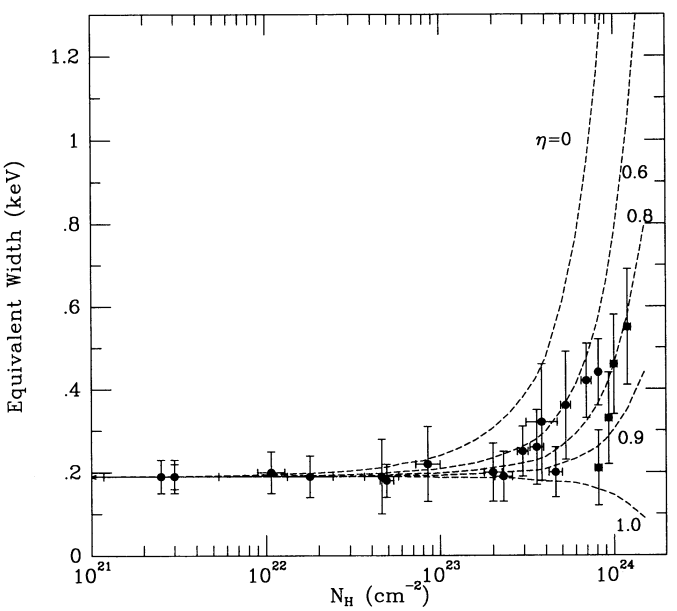

FIG. 8.—Iron line equivalent width versus absorption column density N_H. The dashed curves are expected equivalent widths calculated from eq. (7) for various covering factors η = 0, 0.6, 0.8, 0.9, and 1.0.

a mixture of fluorescent lines from cold (6.4 keV line) and ionized material (6.7 keV line). Although we are unable to derive line width because of insufficient statistics, the iron line flux observed at the bottom of the dip could have same origin as those in low state. However, the iron line flux observed at present for low absorbing column (20 counts s^{-1}) is 4 times higher than that obtained by Mihara et al. (1991) in the low state (3.8 counts s^{-1}). Such high flux cannot be interpreted by stellar atmosphere nor accretion disk edge. For the case of Her X-1 binary system, we can simply estimate the equivalent width of iron line from the companion atmosphere to be $\sim$20 eV (Basko 1978), and that from an accretion disk surface to be $\sim$ 30 eV (Basko 1978). Both of which are far smaller than the observed equivalent width of $\sim$200 eV. The X-ray absorbing clouds at the disk rim are also not enough to explain the observed line intensity, since the solid angle sustained by the clouds is estimated to be $(\Omega/4\pi)_{\rm clouds} < 0.06$, and estimated equivalent width is only $\sim$20 eV even if the clouds have average column density of a few times 10^{23} cm^{-2}. The dependence of iron line flux on absorbing column shown in Figure 7*b* imply that the size of the reprocessing region is comparable to or smaller than those of the absorbing clouds. If the reprocessing region is far larger or far smaller than the absorbing clouds, such a dependence of iron line intensity on $N_{\rm H}$ as seen in Figure 7*b* cannot be expected; it should show a large increase with the increase of $N_{\rm H}$ or should be flat. This suggest that iron lines observed in main-on state are generated on the localized region near the neutron star, such as the Alfvén surface.

The observed line energy of $E_{\rm K} = 6.4$ keV requires that the line emitter should be cold enough to stay in a low ionization state ($\leq$Fe XVIII). In this case the ionization parameter ξ (Tarter, Tucker, & Salpeter 1969; Kallman & McCray 1982) should satisfy the following condition:

$$\xi \equiv \frac{L_x}{nr^2} \leq 80\,, \tag{6}$$

where n is the number density of ambient gas and r the distance from the neutron star. Therefore when we adopt the Alfvén surface region ($r_{\rm A} \simeq 3 \times 10^8$ cm) as the reprocessing site, a gas density $n \geq 1 \times 10^{10}$ cm^{-3} is required to produce the iron line at $E_{\rm K} = 6.4$ keV. It is noted that this reprocessing site should not be intersect the line of sight, otherwise the region leads to absorb soft X-rays of direct beam. The observed result shows a slight increase in the equivalent width at large $N_{\rm H}$ (see Fig. 8). Assuming the covering factor of the iron-line emission region by the obscuring cloud to be η, we can calculate the expected equivalent width by

$$\mathrm{EW} = \frac{I_{\rm Fe}[\eta \exp(-\sigma(E_{\rm K})N_{\rm H}) + (1-\eta)]}{AE_{\rm K}^{-\alpha}[\exp(-\sigma(E_{\rm K})N_{\rm H}) + x]}\,, \tag{7}$$

where $I_{\rm Fe}$ is the iron-line intensity, and x is the ratio of the scattering flux to the direct component. In the calculation, we assume $x = 0.03$ (although some dependence on the $N_{\rm H}$ value is suspected as seen in Fig. 7*c*), the line-center energy $E_{\rm K} =$ 6.4 keV, and the equivalent width to be 0.19 keV at $N_{\rm H} = 0$ (no intervening cloud), respectively. The results are shown in Figure 8 for various values of η. From the scatter of data points, the range of η is estimated to be $0.6 < \eta < 0.9$ with a most probable value of $\eta = 0.8$. Uniform and complete coverage of the iron-line emission region by an intervening cloud is rejected.

This result indicates that $\sim$20% of the iron line reprocessing site is not occulted by the rim cloud even at the time of highest $N_{\rm H}$. This, in turn, suggests that even if the proposed Alfvén shell is the major site of iron line emission that is not obscured by the cloud, outer rim of accretion disk and the companion star atmosphere may be responsible for the additional emission.

4.4. *Summary*

In summary, from the spectroscopic studies of the pre-eclipse dip of Her X-1, we have derived the following results.

1. In spite of the wide variations of intensity during the pre-eclipse phase, which is predominantly due to absorption and scattering, the source luminosity of Her X-1 is nearly constant during the observation at the value $L_x = 2.1 \times 10^{37}$ ergs s^{-1} for $d = 5$ kpc.
2. The spectra observed during the dip can be explained by the superposition of the highly absorbed direct (pulsating) component and the nonpulsating unabsorbed component, in addition to the reprocessed iron emission line.
3. We attribute the absorption of the direct beam to clouds formed around the impact zone of the inflowing stream onto the accretion disk. The vertical turbulence or the perturbation of matter at the impact zone may be responsible for producing the short-time intensity fluctuations at the beginning of the dip and the column density variation during the dip.
4. The nonpulsating unabsorbed component with spectral shape similar to the direct component, which is revealed both from the residual counts seen in the pulse-height ratio and the absence of the pulse shape below $\sim$5 keV during the dip, can be interpreted as the results of scattering of the direct beam. An accretion disk corona, with size is $\sim 2 \times 10^{11}$ cm, explains satisfactorily the characteristics of the scattered component.
5. The iron line energy was predominantly 6.4 keV during the present observation (there was no evidence of a 6.7 keV line), suggesting that the emission arises in a cool region. The correlation between the iron line intensity and absorption column density suggests that the line emission originates mainly from the Alfvén surface; the fluorescence emission is partially obscured by the optically thick gas cloud passing across the line of sight.

We would like to acknowledge all the members of the *Ginga* team for their support in making and analyzing these observations. We also wish to thank H. Inoue, T. Kii and A. C. Fabian for valuable discussion. C. S. C. is grateful to the Japan Society for Promotion of Science for a research fellowship, and also to the Korea Science and Engineering Foundation for supporting his visit to Japan.

REFERENCES

Bahcall, J. N. 1978, in Physics and Astrophysics of Neutron Stars and Black Holes (Amsterdam: North Holland), 63
Bahcall, J. N., & Bahcall, N. A. 1972, ApJ, 178, L1
Basko, M. M. 1978, ApJ, 223, 268
———. 1980, A&A, 87, 330
Bochkarev, N. G. 1989, Soviet Astron., 33(6), 638
Bochkarev, N. G., & Karitskaya, E. A. 1989, Ap&SS, 154, 189
Boynton, P. E., Canterna, R., Crosa, L., Deeter, J., & Gerend, D. 1973, ApJ, 186, 617
Boynton, P. E., Crosa, L. M., & Deeter, J. E. 1980, ApJ, 237, 169

Courvoisier, T. L. J., Parmar, A. N., Peacock, A., & Pakull, M. 1986, ApJ, 309, 265
Crampton, D. 1974, ApJ, 187, 345
Crampton, D., & Hutchings, J. B. 1974, ApJ, 191, 483
Crosa, L. M., & Boynton, P. E. 1980, ApJ, 235, 999
Davidsen, A., Henry, J. P., Middleditch, J., & Smith, H. E. 1972, ApJ, 177, L79
Deeter, J., Boynton, P. E., & Pravdo, S. H. 1981, ApJ, 247, 1003
Deeter, J., Boynton, P. E., Miyamoto, S., Kitamoto, S., Nagase, F., & Kawai, N. 1991, ApJ, 383, 324
Deeter, J., Crosa, L., Gerend, D., & Boynton, P. E. 1976, ApJ, 206, 861
Forman, W., Jones, C. A., & Liller, W. 1972, ApJ, 177, L103
Gerend, D., & Boynton, P. E. 1976, ApJ, 209, 562
Giacconi, R., Gursky, H., Kellogg, E., Levinson, R., Schreier, E., & Tananbaum, H. 1973, ApJ, 184, 227
Gorecki, A., et al. 1982, ApJ, 256, 234
Gruber, D. E., et al. 1980, ApJ, 240, L127
Haberl, F., & White, N. E. 1990, ApJ, 361, 225
Hayashida, K., et al. 1989, PASJ, 41, 373
Hirose, M., Osaki, Y., & Mineshige, S. 1991, PASJ, 43, 809
Howarth, I. D., & Wilson, B. 1983, MNRAS, 204, 1091
Hutchings, J. B., Gibson, E. M., Crampton, D., & Fisher, W. A. 1985, ApJ, 292, 670
Jones, C., & Forman, W. 1976, ApJ, 209, L131
Joss, P. C., Li, F., Wang, Y. M., & Hearn, D. 1977, ApJ, 214, 874
Kallman, J. R., & McCray, R. 1982, ApJS, 50, 263
Katz, J. I. 1973, Nature Phys. Sci., 246, 87
Makino, F., & Astro-C team 1987, Ap. Letters Comm., 25, 223
Makishima, K., et al. 1990, PASJ, 42, 295
Makishima, K., & Mihara, T. 1992, in Frontiers of X-Ray Astronomy, ed. Y. Tanaka & K. Koyama (Tokyo: Universal Academy), 23
Mason, K. O. 1986, in The Physics of Accretion onto Compact Object, ed. K. O. Mason, M. G. Watson & N. E. White (New York: Springer), 249
Middleditch, J. 1983, ApJ, 275, 278
Middleditch, J., & Nelson, J. 1976, ApJ, 208, 567
Mihara, T., et al. 1990, Nature, 346, 440
Mihara, T., Ohashi, T., Makishima, K., Nagase, F., Kitamoto, S., & Koyama, K. 1991, PASJ, 43, 501
Milgrom, M., & Salpeter, E. E. 1975a, ApJ, 196, 583
———. 1975b, ApJ, 196, 589
Morrison, R., & McCammon, D. 1983, ApJ, 270, 119
Nagase, F. 1989, PASJ, 41, 1
Nagase, F., et al. 1992, ApJ, 396, 147
Ohashi, T., et al. 1984, PASJ, 36, 719
Parmar, A. N., Pietsch, W., McKechnie, S., White, N. E., Trumper, J., Voges, W., & Barr, P. 1985, Nature, 313, 119
Parmar, A. N., White, N. E., Giommi, P., & Gottwald M. 1986, ApJ, 308, 199
Pravdo, S. H., Becker, R. H., Boldt, E. A., Holt, S. S., Serlemitsos, P. J., & Swank, J. H. 1977a, ApJ, 215, L61
Pravdo, S. H., Boldt, E. A., Holt, S. S., & Serlemitsos, P. J. 1977b, ApJ, 216, L23
Pravdo, S. H., et al. 1978a, ApJ, 225, L53
———. 1978b, ApJ, 225, 988
Priedhorsky, W. R., & Holt, S. S. 1987, Space Sci. Rev., 45, 291
Roberts, W. J. 1974, ApJ, 187, 575
Soong, Y., Gruber, D. E., & Rothschild, R. E. 1987, ApJ, 319, L77
Soong, Y., Gruber, D. E., Peterson, L. E., & Rothschild, R. E. 1990, ApJ, 348, 641
Tananbaum, H., Gursky, H., Kellog, E. M., Levinson, R., Schreir, E., & Giacconi, R. 1972, ApJ, 174, L143
Tarter, C. B., Tucker, W. H., & Salpeter, E. E. 1969, ApJ, 156, 943
Trümper, J., Kahabka, P., Ögelman, H., Pietsch, W., & Voges, W. 1986, ApJ, 300, L63
Trümper, J., et al. 1978, ApJ, 219, L105
Tsunemi, H., Kitamoto, S., Manabe, M., Miyamoto, S., Yamashita, K., & Nakagawa, M. 1989, PASJ, 41, 391
Tueller, J., et al. 1984, ApJ, 279, 177
Turner, M. J. L., et al. 1989, PASJ, 41, 345
Ushimaru, N., Tawara, Y., & Koyama, K. 1989, PASJ, 41, 441
Voges, W., Pietsch, W., Reppin, C., & Trümper, J. 1982, ApJ, 263, 803
White, N. E., Swank, J. H., & Holt, S. S. 1983, ApJ, 270, 711